Hybrid simulation with online model updating: application to a reinforced concrete bridge endowed with tall piers

Zhu Mei[2], Bin Wu[1, 2,*], Oreste S. Bursi[3], Guoshan Xu[2], Zhen Wang[2], Tao Wang[4], Xizhan Ning[2]

[1] *School of Civil Engineering and Architecture, Wuhan University of Technology, Wuhan 430070, China*

[2] *School of Civil Engineering, Harbin Institute of Technology, Harbin 150090, China*

[3] *Department of Civil, Environmental and Mechanical Engineering, University of Trento, Via Mesiano 77, 38123 Trento Italy*

[4] *Key Laboratory of Earthquake Engineering and Engineering Vibration, Institute of Engineering Mechanics, China Earthquake Administration, Harbin 150080, China*

ABSTRACT

Hybrid (numerical/physical) simulation (HS) with both numerical (NS) and physical substructures (PS) is proposed to investigate the seismic behavior of a complex reinforced concrete (RC) rigid frame bridge with tall piers characterized by thin-wall hollow sections. The HS primarily intends to increase the knowledge on the seismic performance of RC tall piers with thin-walled hollow sections. In order to reduce modeling errors of parts numerically simulated, i.e. NSs, we propose a novel hybrid simulation with online updating (UHS) of concrete constitutive parameters provided by PS data. In particular, the unscented Kalman filter (UKF) embedded in the OpenSees software is proposed for parameter identification. The online updating UHS with this identification method is numerically validated on a one-bay one-story frame. Then, applications of UHS are applied to a RC bridge. Results show that the proposed parameter identification and the relevant HS with online updating exhibit both a favorable performance and robustness with respect to standard techniques (SHS) without model updating. With regard to the seismic response of the simulated bridge, both the damage evolution and the failure modes of the PS are presented. Though both flexural and shear behavior characterize PS failure, an unfavorable shear failure was followed by stirrup fracture.

KEY WORDS: RC rigid frame bridge; tall pier; thin-walled hollow section; OpenSees, parameter identification; online model updating hybrid simulation (UHS); unscented Kalman filter

1. INTRODUCTION

1.1 Background and motivation

Rigid frame RC bridges with tall piers have been constructed mainly in mountainous area, due to its good spanning ability to cross deep canyons. A hollow cross-section is particularly common for the design of RC tall piers since it can provide sufficient stiffness with a reduced cross-section area which brings the benefit of cost savings, and the reduction of pier mass resulting in the attenuation of the relevant seismic response. In addition, a hollow section makes piers more flexible thus decreasing early cracks induced by thermal stresses due to hydration heat. However, damage investigations after major earthquakes show that a few RC columns with hollow section were severely damaged due to insufficient shear strength [1][2]. Hence, it is necessary to employ reliable experimental data to understand and design rigid

frame RC bridges with tall piers and hollow cross-section. In this respect, quasi-static testing is the most widely used method [2]-[5]. Though both vertical and bilateral horizontal loads can be involved in [5], given the fact that loading histories in quasi-static testing are regularly pre-determined according to yield quantities of the specimen, quasi-static testing is not capable of generating realistic earthquake loading histories. Thus, due to the possibility of simulating more realistic seismic loading histories and involving effective member sizes, hybrid (numerical/physical) simulation can represent a fairly good approach for reproducing the dynamic response of bridges subjected to earthquakes. However, limited research on HS of bridges can be found. Spencer et al. carried out a series hybrid simulation on a bridge with common-height RC piers whose cross-section are circle and solid [6]. Pegon and Pinto implemented the substructuring HS on an RC bridge with thin-wall hollow-section piers. While in this study case, the pier is also a common-height pier whose height is 28m [7]. Terzic and Stojadinovic adopt HS for investigating the bridge response to the earthquake excitation followed by truck load. In this study, the experimental pier is solid circle-section [8]. In the researches [6] to [8], it is all assumed that the NS is accurate. Abbiati et al. employed HS for assessing the seismic behavior of an old RC viaduct [9], where the finite element model of the NS is pre-justified using the experimental data obtained from quasi-static tests of small-scaled piers. This means, before the HS, several quasi-static tests have to be carried out firstly.

HS benefits from both computation and testing. As shown in Fig.1(a), the computer: (i) solves the system of equations of motion; (ii) simulates both inertial and damping forces in the system of equations. The testing technique: collects the nonlinear restoring forces of the structure from the physically tested structure. HS with substructures, as shown in Fig.1(b), allows for the key region (or component) of a structure, known as PS which is experimentally tested, being isolated from the remainder of the structure, referred to as the NS, which is numerically simulated [10]. As only one or several parts of the whole structure can be really tested, HS is a relatively economic way for investigating the seismic behavior of a structure at a large or even full scale (PS). Nonetheless, for a multi-pier bridge, it is impractical to physically test all piers; thus, most of the piers that may undergo strong nonlinearities have to be numerically simulated. As a result, the reliability of modeling nonlinear critical members as NS can be undermined.

When numerical models can only be set based on known assumptions, e.g. type of elements, constitutive models, time-stepping methods, etc., online model updating represents an appropriate and effective way, to improve the accuracy of NSs. As they affect the accuracy of numerical simulation, constitutive models at different levels are extensively investigated for finite element (FE) software [11][12]. Consequently, researchers involved in HS are analyzing in depth the identification of constitutive models with limited parameter numbers.

The three levels of constitutive models involved in mechanics are the component level characterized by a force-displacement relationship, the section level with a moment-curvature relationship and the material level characterized by a stress-strain relationship. As regards model updating in HS, the investigation extensively focused on the component constitutive model [13]-[15], where the displacement and force relationships are directly employed for critical members. This results in difficulties in updating parameters for the different boundary conditions, geometric dimensions of RC members, reinforcement ratios, axial compression ratios, etc. As a result, Wu et al. [16] proposed to identify the parameters of the constitutive model at the section level of steel members and applied model updating. However, focusing on a constitutive model at a sectional level can only solve the updating problem of structural members with different size along the length direction. Those with different areas of cross section, axial ratios, boundary conditions, etc., cannot be treated. Moreover, for both the constitutive models at a global level and those at the sectional level, the intra-element

responses of a structural member cannot be captured. Thus, owing to their insufficient accuracy, these two types of constitutive laws are not commonly used in state-of-the-art modeling of civil-engineering structures. Conversely, a fiber-based model characterized by stress-stain relationships is certainly more accurate and frequently used to simulate the distributed plasticity of RC members. Moreover, targeting at the stress-strain relationship, the strict conditions, such as geometric, loading and boundary conditions, do not need to comply with between PS and NS. Therefore, model updating should be more effective when applied to a material level of a constitutive model.

To implement model updating in HS with the presence of the nonlinear hysteretic behavior of a member/system, the identification method has to satisfy two conditions: (i) it has to be an online method; (ii) it must deal with a nonlinear system. In this respect, the recursive least square estimation (RLS) only applies to linear or piecewise linear systems. Kalman filter (KF) [16], which is still applicable to linear systems [17][18], extends the RLS to the region of time-varying systems by adding a state predictor to the RLS based on a state-space model. In order to solve the problem of estimation of nonlinear systems, the extended Kalman filter (EKF) [19] and the unscented Kalman filter (UKF) [20]-[22], have been proposed, respectively, and been widely used [23]-[27]. As a result, many studies [20]-[22][28][29] found that the UKF is superior to the EKF and provides more robust results for strong nonlinear system without the need of Jacobian operators. Furthermore, to reduce the computing time of the entire hybrid simulation with model updating, the module for parameter identification has to be computationally efficient. The comparison between the particle filter (PF), also known as the sequential Monte Carlo method [30], the genetic algorithms [31] and the UKF, entails that UKF can provide a sufficient estimation accuracy with low time burden. Thus, the UKF is adopted for parameter identification of RC members in this paper.

More precisely, the UKF is used for the estimation of parameters based on the difference between estimated and measured values of observed quantities. As a result, besides other factors that influence parameter convergence, such as types of input, complexity of the target model, etc., the observation should be sufficiently sensitive to parameters subject to identification. The stress level is the first choice for the identification of parameters at the material level [31]. However, for RC structures, it is difficult to accurately measure concrete stresses, especially after concrete cracking. In addition, the common measurement in HS is the restoring force of a component which is proven to be sufficiently sensitive to parameters [32]. Therefore, it is reasonable to take force values as observed quantities for identification [33]. Hence, other difficulties occur because measurement equations which describe the relationships between parameters to be identified and the observations are difficult to express in an analytical manner. To solve this problem, an FE model is proposed to embed into the UKF to represent the measurement equations. As open-source software platform, the OpenSees [34] is used both for parameter identification and updating. Therefore, NSs are modelled in OpenSees in this paper.

1.2 Scope

In this paper, we propose an HS method with model updating of parameters of constitutive models, where parameters are identified by the UKF and updated to models in NSs. In order to implement UKF, the OpenSees software was properly modified to compute estimated measurements. Along these lines, Section 2 presents how UKF was implemented, in view of parameter identification of material constitutive models. Moreover, the framework of updating HS is introduced in Section 3 and, to validate the UKF implementation, a monotonic

static test on an RC column was carried out. Successively, the updating HS was numerically verified on a simple RC frame in Section 3. Then, in Section 4, both standard HS without model updating (SHS) and HS with model updating (UHS) are implemented and used for a RC rigid frame bridge to show both the effectiveness and accuracy of the novel method. As a result, the seismic response of the simulated bridge, its damage evolution and relevant failure modes of piers are presented and commented.

2. UKF FOR PARAMETER IDENTIFICATION AND VALIDATION

2.1 Parameter identification method

Let's assume that the parameter vector of the constitutive model, $\mathbf{x}$, and the measurement vector, $\mathbf{y}$, are related by the following equation which is called the measurement model,

$$\mathbf{y} = \mathbf{h}(\mathbf{x}) + \mathbf{v} \tag{1}$$

where $\mathbf{y}$ is an m-dimensional measurement vector, and $\mathbf{v}$ a measurement noise vector. Doob [35] proved that the optimal estimation of a random vector $\mathbf{x}$ with the mean-square-error criterion is the conditioned mean given $\mathbf{y}$, which is just the Bayesian estimation.

For linear systems, *i.e.* when $\mathbf{h}$ is a linear function, the KF [17] can exactly provide this optimal estimation and requires only the first two orders of statistic moments about $\mathbf{x}$ and $\mathbf{y}$. By calculating the secondary moment, the Kalman gain can be calculated as follow,

$$\mathbf{K}_i = \mathbf{P}_{\mathbf{xy},i}\left(\mathbf{P}_{\mathbf{yy},i} + \mathbf{R}\right)^{-1} \tag{2}$$

where, $\mathbf{K}_i$ is the Kalman gain, $\mathbf{P}_{\mathbf{yy},i}$ is the variance of $\mathbf{y}$, $\mathbf{P}_{\mathbf{xy},i}$ is the covariance of $\mathbf{x}$ and $\mathbf{y}$, and $\mathbf{R}$ is the variance of the measurement noise $\mathbf{v}$. Then the optimal estimation of $\mathbf{x}_i$, *i.e.* the conditional mean, which is the first moment of $\mathbf{x}_i$, given $\mathbf{y}_i$, $\mathbf{y}_{i-1}$ …$\mathbf{y}_1$, can be calculated as follow,

$$\hat{\mathbf{x}}_i = \hat{\mathbf{x}}_{i-1} + \mathbf{K}_i\left(\mathbf{y}_i - \hat{\mathbf{y}}_i\right) \tag{3}$$

where, $\hat{\mathbf{y}}_i$ is the estimation of the measurement $\mathbf{y}_i$.

For nonlinear systems, the exact optimal estimation can only be computed when the conditional probability distribution of $\mathbf{x}$ given $\mathbf{y}$ is known. However, it is usually difficult to obtain the knowledge of this distribution *a priori*. Hence, in order to obtain a sub-optimal estimation with an acceptable precision at a reasonable cost, it is worthwhile to extend the KF to nonlinear systems. One of the most widely used method is the UKF which provides an estimation with an acceptable error; it is based on the following approximations: i) it retains the linear structure of the KF, *i.e.* the recursive estimation frame; ii) it uses the first two orders of statistic moments to obtain the Kalman gain, though it is not sufficient for nonlinear systems; iii) it approximates the first two orders of statistic moments themselves.

The core of the UKF is the unscented transformation (UT) with the deterministic sampling method [20][21], which is the method for estimating the measurements, *i.e.* $\hat{\mathbf{y}}_i$ in Equation (3) and the covariance matrices $\mathbf{P}_{\mathbf{yy},i}$ and $\mathbf{P}_{\mathbf{xy},i}$ in Equation (2). Though $\mathbf{h}$ is nonlinear, the $\hat{\mathbf{y}}_i$ can also be approximated through the UT with the deterministic sampling method on the condition that $\mathbf{h}$ is known and can be analytically expressed. However, the $\mathbf{x}$ to be identified, in this work, is the vector of parameters of a concrete constitutive model, while the measurement vector $\mathbf{y}$ is represented by the restoring force vector in a HS. This indicates that

the relation of **x** and **y** can hardly be expressed in an analytical form. As a result, this leads to the difficulties for calculating the estimation of measurement, $\hat{\mathbf{y}}_i$, for that the corresponding sampling points which are the intermediate quantities for computing the estimated measurement can hardly be calculated. In detail, the sampling points of **x** with the scaled symmetric unscented transformation can be expressed as [20][21],

$$\boldsymbol{\chi}_j^i = \begin{cases} \hat{\mathbf{x}}_{i-1}, & j=0 \\ \hat{\mathbf{x}}_{i-1} \pm \alpha \left(\sqrt{n\mathbf{P}_{\hat{\mathbf{x}}\hat{\mathbf{x}}}^i} \right)_j, & j=1,2,...n \end{cases} \tag{4}$$

where n is the dimension of **x**, $\boldsymbol{\chi}_j^i$ are the sampling points which are also called sigma points whose total number is $2n+1$ at the i-th step. Based on the known **h**, one can find the corresponding $\boldsymbol{\xi}_j^i$ points of **y**,

$$\boldsymbol{\xi}_j^i = \mathbf{h}\left(\boldsymbol{\chi}_j^i, \mathbf{r}_{i-1}, \mathbf{u}_i\right) \tag{5}$$

where $\mathbf{u}_i$ is a vector of displacements as an input. Note that, the $\boldsymbol{\xi}_j^i$ points are the intermediate quantities for calculating the $\hat{\mathbf{y}}_i$. To solve the problem that the **h** can hardly be expressed in an analytical form, the OpenSEES finite element software is employed to calculate the corresponding points $\boldsymbol{\xi}_j^i$, as shown in Fig. 2; then the measurements can be estimated by the formula provided by UKF which is executed in Matlab software [36]. In particular, W_j is the weight factor of each $\boldsymbol{\xi}_j^i$; $\mathbf{e}_i$ is the difference of the measurement vector and its estimation, *i.e.* $\mathbf{e}_i = \mathbf{y}_i - \hat{\mathbf{y}}_i$. Please, note that $\mathbf{r}_{i\text{-}1}$, shown in both in Eqn. (5) and Fig. 2, is defined as the vector of historical variables at time i-1, which is the vector including all those variables that influence the analysis results at next time step i. In this case, $\mathbf{r}_{i\text{-}1}$ is the vector of the variables generated by the OpenSEES computation at Step i-1. Clearly, the nonlinear transformation of the $2n+1$ sigma points $\boldsymbol{\chi}_j^i$ at each time step i is based on the same history variable $\mathbf{r}_{i\text{-}1}$ to finally attain the estimated measurement $\hat{\mathbf{y}}_i$. Therefore, an extra running of the OpenSEES with the new estimated parameters at step i, *i.e.* $\hat{\mathbf{x}}_i$, is executed to obtain the unifying historical variables for the next step.

2.2 Uniaxial constitutive model of concrete

The constitutive model adopted for simulating the nonlinear behavior of concrete in OpenSees is a combination of the Kent-Park model [37] and the Scott-Park model [38], named the Kent-Scott-Park model [39]. The stress-strain relation of this model, shown in Fig. 3, is controlled by four parameters, where f_c is the axial compressive strength, ε_0 is the strain at the compressive strength, ε_m is the crushing strain, and f_r is the strength when the strain is equal to or greater than ε_m. This constitutive model of concrete is applicable for both the unconfined and confined concrete by determining different values of parameters.

For multi-piers bridge, it may happen that the confinement ratios of concrete are different from one pier to another. This may lead to a situation that the constitutive parameters of confined concrete model identified with the PS data cannot be directly updated to the confined concrete model in the NS, when only one or two piers can be taken out as the PS. As the parameters of unconfined concrete model are the same for both the PS and NS, we seek to build the connection between the confined concrete model for PS and that for NS by unifying the model of confined concrete and of unconfined concrete.

From existing research works [37][38], it can be concluded that the parameters of confined concrete are related to those of unconfined concrete through the volumetric ratio of stirrup, ρ_s, by,

$$f_c = (1 + K_{sr1} \cdot \rho_s) f_{cu} \tag{6}$$

$$\varepsilon_0 = (1 + K_{sr2} \cdot \rho_s) \varepsilon_{0u} \tag{7}$$

$$\varepsilon_m = (1 + K_{sr3} \cdot \rho_s) \varepsilon_{mu} \tag{8}$$

where, f_{cu}, ε_{0u} and ε_{mu} are the parameters of unconfined concrete; f_c, ε_0 and ε_m are the parameters representing the confined concrete when $\rho_s \neq 0$, and unconfined concrete when $\rho_s = 0$. The proportional factor $K_{sr1} = f_{yh} / f_c$, where f_{yh} is the yield strength of stirrups. For the second proportional parameter K_{sr2}, Kent [37] recommends that $K_{sr2} = K_{sr1}$, while Mander [40] suggests $K_{sr2} = 5K_{sr1}$. About K_{sr3}, Mander recommends $K_{sr3} = 0.9 f_{yh} / (300 \times 0.004)$, while Kent proposes a more complicated approach. In addition, the crushing strength is generally assumed as a fraction of the compressive strength, that is $f_r = K f_c$, where Hognestad [41] suggests K = 85%. Other researchers prefer figures such as 80% or 50% based on experimental data. As a result, the stress-strain can be expressed by means of seven constitutive parameters and the volumetric ratio of stirrups as,

$$\begin{cases} \sigma = (1 + S_1 \cdot \rho_s) f_{cu} \left[\dfrac{2\varepsilon}{(1 + S_2 \cdot \rho_s)\varepsilon_0} - \left(\dfrac{\varepsilon}{(1 + S_2 \cdot \rho_s)\varepsilon_0} \right)^2 \right] & \text{Increasing branch} \\ \sigma = (1 + S_1 \cdot \rho_s) f_{cu} + k \cdot \left[\varepsilon - (1 + S_2 \cdot \rho_s)\varepsilon_0 \right] & \text{Decreasing branch} \end{cases} \tag{9}$$

whose simplified form can be written as,

$$\sigma = g(\varepsilon, f_{cu}, \varepsilon_{0u}, \varepsilon_{mu}, K, K_{sr1}, K_{sr2}, K_{sr3}, \rho_s) \tag{10}$$

So far, the concrete constitutive model adopted in this paper is characterized by seven parameters to be identified. A parameter sensitivity analysis has been carried out to analyze the influence of the seven parameters on the restoring force of a RC column [33]. Relevant results indicate that the force is mainly sensitive to f_{cu}, ε_{0u} and K.

2.3 Validation of the identification method

The OpenSees embedded UKF was validated through a monotonic loading test of a RC column with a height of 1.2m. The cross section of the column, the test setup and other details can be found in [33].

The recommended values of parameters, mentioned in Subsection 2.2 are adopted to be the initial values of parameters for the identification with UKF. In order to deal with more reliable values, the material tests of concrete and stirrup are carried out firstly to obtain f_{cu} and f_{yh}. The initial values of K_{sr1} and K_{sr3} can be calculated with the formulas recommended above. With regard to K_{sr2}, its initial value is evaluated as three times of K_{sr1}, where three is a mean value. The initial values are listed in Table 1 and the initial covariance matrices for UKF read $\mathbf{P}_{\hat{x}\hat{x}}^0 = \text{diag}\,[2.7 \times 10^{-2}, 3.5 \times 10^{-6}, 5 \times 10^{-4}]$ and $R = 9 \times 10^{-4}$, respectively.

For the space limitation, only the identification result of the most sensitive parameter f_{cu} and the comparison of displacement-force relations are presented in Fig. 4. For the other parameters, please refer to [33]. Testing results show a favorable performance of the identification method. However, a careful reader can observe that the parameter f_{cu} jumped from an initial value of -43 MPa to -90MPa, in the first few steps. This was caused by the

Kent-Scott-Park model which ignores the tensile strength of concrete which plays a significant role in the restoring force of a flexural member when the loading does not entail cracking. If it is ignored, to compensate for the loss of tensile strength, the UKF method forces f_{cu} to increase. The minus in Fig. 4(a) indicates that the stress is a compressive stress.

3. HYBRID SIMULATION WITH ONLINE MODEL UPDATING

Both standard hybrid simulation without model updating (SHS) and with model updating (UHS) rely on a COORDINATOR that runs in one computer which is in charge of solving the dynamic equations of motion and the analyzing of the NS. The actuator controller is managed by the MTS793 software which is installed in another computer. Moreover, the Matlab software host the module for parameter identification of UHS in a third computer. Data transferring between the three computers are managed by the Coordinator through a TCP/IP protocol.

3.1 Framework of UHS

In order to run the SHS, the system of equations of motion of the whole (emulated) system,

$$\mathbf{M}\ddot{\mathbf{u}}(t)+\mathbf{C}\dot{\mathbf{u}}(t)+\mathbf{R}(t)=\mathbf{F}(t) \tag{11}$$

is solved by standard time-stepping schemes, like the central difference method, Newmark-β method, etc. In (11), the inertia force $\mathbf{M}\ddot{\mathbf{u}}(t)$ and the damping force $\mathbf{C}\dot{\mathbf{u}}(t)$, are numerically simulated, while the restoring force, $\mathbf{R}(t)$ is measured from the tested structure whose displacement loading commands are those solved by the integration method at time t. $\mathbf{F}(t)$ defines the input ground motion. For a SHS with substructures, the system is divided into PSs and NSs, as shown in Fig. 5. Then, the computed displacements are separately sent to the substructures. Accordingly, $\mathbf{R}(t)$ is split into the restoring force of PSs, $\mathbf{R}_e(t)$, and NSs, $\mathbf{R}_n(t)$. In detail, the sum of the $\mathbf{R}_e(t)$ and the $\mathbf{R}_n(t)$ at the DoFs of node 3 are the final restoring forces of Node 3. For the other DoFs, the $\mathbf{R}_n(t)$ is the final restoring force. The schematic of SHS without model updating can be understood from Fig. 5.

By adding an online model updating module, see Fig. 5, to the SHS, the enhanced UHS can be achieved. The key problem of model updating is the parameter identification part where an extra numerical model of the PS is needed. In this part, the parameters of the constitutive model in the FE model of the PS are adjusted/optimized based on a certain criterion to minimize the deviation of the restoring forces between estimated and measured values. To improve the accuracy of the NS, then, these optimized parameters are sent to the numerical members which are simulated with the same constitutive model as the PS, and updated. The COORDINATOR shown in Fig. 5 has three basic functions, i) to solve the system of equations of motion; ii) to control the entire process of testing; iii) to cope with data transmission of each module.

3.2 Numerical validation

In order to validate the feasibility and stability of the whole process of UHS, a case study made of a RC frame was implemented. Three cases, as illustrated in Fig. 6, are involved in the

numerical verification: (i) Case A is a reference case in which the concrete constitutive parameters are the same for the two columns and taken as the true parameters for reference; (ii) Case B is the SHS case in which the left column is considered as the PS and the same as that in Case A, while the concrete parameters in the right column are different from those in the PS; (iii) Case C is a UHS case in which the left column is the PS, and the right column is the NS for parameter updating. That is, the initial values of the concrete parameters of the NS in Case C are the same as those in the right column of Case B, and then it is updated using the identified values.

The initial covariance matrix and measurement noise variance of $\mathbf{x}$ read $\mathbf{P}_{\hat{x}\hat{x}}^{0} = \mathrm{diag}\,[1.279, 0.587, 16.5]$ and R=100, respectively. The initial values of the seven constitutive parameters involved in (10) are presented in the second row of Table 2. More precisely, f_{cu}, ε_{0u} and K are the three parameters to be identified, whilst the remaining ones remain unchanged during hybrid simulation. Results of the UHS are shown in Fig. 7-9 and highlight the accuracy improvement of the NS during UHS. Fig. 7 shows that the parameters converge to the reference values pretty fast, making the displacement at the top of numerical column and the hysteretic loops of Case C very close to those obtained in Case A, as shown respectively in Fig. 8 and Fig. 9. In Fig. 8 one can observe that the relative errors achieved by UHS are rather small. It is noted that, in this case there is only one NS which needs to be updated. As the number of NSs increases, we expect that the improvement of accuracy of the UHS will be more significant.

In order to show result robustness to initial values of constitutive parameters, a number of hybrid simulations are carried out considering parameter uncertainties. The results are presented by means of the bar chart diagram depicted in Fig. 10. More precisely, the x-axis represents the errors of the maximum displacement at the top of the RC frame between Case A, i.e. the reference case, and Case C, i.e. the UHS. The y-axis identifies parameters.

The base value of the displacement error is the one obtained from the numerical example of the RC frame, which is 0.87%, and is identified by the vertical dashed line. The initial values of parameters are shown in the second row of Table 2 and are, hereafter called, reference initial values (RIVs). For each parameter, two more runs of hybrid simulation are carried out with the initial value of RIV±s.d., while the other six parameters remain unchanged with the initial value of RIV. Because we assumed that the strength level of concrete is C40, the mean value of f_{cu} is 50MPa with a s.d. of 6MPa. Therefore, two more runs were carried out with the initial value of f_{cu} equal to 56MPa and 44MPa, respectively. Likewise for normal concrete, the s.d. of ε 0u is 0.0005，so the two initial values considered were 0.002±0.0005. For the s.d. of remaining parameters, see third row of Table 2, the interested reader can refer to [33].

Results of Fig. 10 clearly emphasize both the robustness and reliability of UHS when parameters of concrete constitutive law are involved. In particular, the robustness of structural responses to the initial values of parameters is pretty good with a maximum error of 4.2%. In addition and for identification, structural responses are most severely affected by the initial value of K.

The average runtime of each identification step is about 0.15s which is a quite small value. The execution time of the FE model is 21.9% of the whole simulation time. Nonetheless, the main factor impacting the execution time is the data transmission between different pieces of

software, i.e the Matlab and OpenSees softwares; The relevant time is 25.9% which is larger than that employed by the FE model computation. In usual non-real-time hybrid simulations presented here, the requirements for the execution time of parameter identification is not so strict. Therefore, the proposed method can cope with requests.

4. HYBRID SIMULATIONS OF A RIGID FRAME BRIDGE

Two cases of HSs were carried out on the RC rigid frame bridge: one for the standard case without model updating (SHS) and the other one for the case with model updating (UHS). One specimen was built for both the two cases. The sequence of the HSs carried out is the standard HS, then the HS with model updating.

4.1 Bridge prototype

The prototype target bridge was the RC continuous bridge shown in Fig. 11. The main bridge was endowed with two tall piers of 126.06m and three spans of 90m, 170m and 90m, respectively.

The cross section of the box girder was variable as presented in Fig. 12. The right part shown in Fig. 12 is the section with a height of 3.7m for the mid span as well as tail beam; while the left part is the section at the root of the beam with a height of 10.0m. The height between them obeyed to a parabola with 1.75 power. The cross section of the main pier was a rectangular hollow section with a thin wall of 0.8m thick. Details are presented in Fig. 13, where the length of the section along the longitudinal direction is constant, i.e. 12m; and the width along the transverse direction is variable with 6.7m at the top of the pier and 10.7m at the bottom. The two main piers were the same and partitioned into five hollow segments with four diaphragms. The total height of each pier was 126.06m with the height of the top hollow segment equal to 26.06m and the others equal to 25m, respectively.

4.2 Testing program

For both the SHS and UHS, a total of eighteen DoFs were considered by lumping six mass points distributed along the pier as presented by Nodes 2, 4, 6, 8, 10 and 12 in Fig. 14. The gravities of the superstructure and the piers were considered by applying vertical loads to each mass point.

As shown in Fig. 14, the substructure with a height of 31.2m from the bottom of the left pier was assumed as PS, while the remaining part is numerically simulated in OpenSees, *i.e.* the NS. The generalized forces of node 2 along three directions, i.e. the lateral force, the vertical force and the bending moment in plane, were the sum of those attained from the NS and measured from the PS. The generalized forces in the other DoFs were only numerical forces.

The NS was a full-scale FE model; while the PS was a 1:12 scaled specimen built and

tested in the Structural and Seismic Testing Center, Harbin Institute of Technology. As a result, the system (11) was solved by the COORDINATOR at full scale. So, the generalized deformations sent to the PS via the controller and the generalized forces which were measured, were scaled according to the similitude ratio S=1/12. Correspondingly, the scaled factors used for data transfer were collected in Table 3.

4.3 Bridge model and NSs

In order to ensure the quality of the FE model of the NS, a refined FE model of the whole bridge was set in OpenSees using force-based beam elements, which was validated by means of bridge field test data. Then, this refined FE model was simplified to increase the computational efficiency of the HS.

A sketch of the refined FE model is illustrated in Fig. 15. With regard to piers, each hollow segment was modeled by three beam elements with a total number of thirty elements; while the box girder was divided into four parts with eight elements per part. Both deck and piers with tapered cross-section were simulated by piecewise equal subsections as shown in Fig. 16. For instance, the approximation of element 1-101 is illustrated in Fig. 16(a). Its width in the approximated model was the mean of the width at node 1 and 101 in the prototype, respectively.

The constitutive model of steel bars and concrete adopted in the FE model were the Giuffre-Menegotto-Pinto model (Steel02 in OpenSees), and the Kent-Scott-Park model (Concrete01 in OpenSees) as mentioned in Subsection 2.2, respectively. Their parameters are listed in Table 4.

The computed frequencies obtained from the refined model are collected in Table 5, and, for the sake of comparison, the field-tested frequencies of the bridge [42] are also listed. As the FE model was a 2D model, only the frequencies along the longitudinal and vertical directions are presented. One can observe that the agreement is favorable.

In order to reduce the complexity and the computational burden of the HS, a simplified FE model with less elements was built using the same material parameters as illustrated in Fig. 17. By applying the same seismic loading, i.e. the El Centro (NS, 1940), to the refined and simplified FE models, the time history analysis results of displacement at the top of one pier are compared in Fig. 18. Because the simplified model can provide accurate results, the relevant NS, except element 1-2 that corresponds to the PS, was used in HS.

4.4 The PS

The main characteristics of the specimen, *i.e.* the PS, are shown in Fig. 19, where both the standard hollow section and the diaphragm sections are presented. The thick of the standard section was only 70mm, and the ratio of the thick and length of the section along the longitudinal direction was 0.07.

The testing setup is presented in Fig. 20; it was characterized by an L-type loading beam connected to the top beam of the specimen, and two portal frames for constraining the out-of-plane displacements. Three MTS actuators, one in the horizontal direction and two in the vertical direction, were used to impose displacements and rotation at the top of the

specimen. The three actuators were controlled by the MTS Flex Text 60 controller which was managed by the MTS793 software.

In order to assure that the target displacement was fully imposed, an outer-loop displacement control was applied to the specimen. With this respect, five displacement sensors, i.e. Linear Variable Differential Transformers (LVDTs), were set up as illustrated in Fig. 21. LVDT1 was for the lateral displacement of the foundation; LVDT2 was for the displacement of the pier top; the difference displacement of the two LVDTs was believed to be the displacement that the top pier really experienced. LVDT5 was for the vertical displacement of the pier top; LVDT3 and LVDT4 were for the vertical displacements of the top beam at the positions corresponding to Actuator2 and Actuator3, respectively. Meanwhile, the combination of LVDT3 and LVDT4 were for the rotation of the top pier.

4.5 Parameter identification

According to Subsection 2.1, $\mathbf{x}$ is used to define the state vector including the concrete constitutive parameters being identified, i.e. $\mathbf{x} = [f_{cu}, \varepsilon_{0u}, K]$, in which the three parameters are the most sensitive ones to the restoring force used in Section 3; $\mathbf{y}$ is adopted for the measurement vector, a scalar quantity in this case, which represents the lateral restoring force of the PS at each step. As shown in Fig. 20, the observation of the lateral restoring force of the PS is measured by Actuator #1. Since we use an Opensees FE model of the PS, the expression of the measurement equation, $\mathbf{h}$, i.e. the measurement equation which describes the relationship of the concrete constitutive parameters being identified and the measurements of the restoring force, the discrete-time state-space model of the measurement equation, can be expressed as,

$$y_k = \mathrm{OSFM}(\mathbf{x}_k, \mathbf{u}_k) + v_k \tag{12}$$

where OSFM stands for the OpenSees FE model. u_k defines the displacement input at each step k of the DoF at the top of the PS, which is received from the COORDINATOR, i.e. $u_k = [d_L, d_V, \theta]$. More precisely, d_L represents the lateral displacement, d_V the vertical displacement, θ the rotation. v_k is a scalar that defines the measurement noise.

The initial covariance matrix of $\mathbf{x}$, $\mathbf{P}_{\hat{x}\hat{x}}^0$, and the measurement noise variance, R, read $\mathbf{P}_{\hat{x}\hat{x}}^0 =$ diag [2.88×10-7, 8.46×10-11, 3.06×10-9] and R = 1×10-3, respectively. The values of these two quantities remain constant for all hybrid simulations of the bridge subjected to the earthquake records with different peak ground acceleration (PGA). The detailed PGA levels are provided hereinafter.

4.6 Results

4.6.1 Results of parameter identification

The earthquake record of the El-Centro (NS, 1940) was adopted as seismic loading with a peak ground acceleration (PGA) scaled to 0.07g, 0.22g, 0.4g, 0.62g, 1g and 1.5g. In the case of SHS, the PS failed at a PGA = 1.5g. Therefore, there was no results for the UHS at PGA =

1.5g. For the other PGA levels, a favorable performance of the proposed identification method can be found. For brevity, only the results at a PGA = 1.0g are shown in Fig. 22 and Fig. 23. The comparisons of displacement-force relationship between SHS and HS with model updating (UHS) are shown in Fig. 24.

From Fig. 22, one careful reader can observe that the identified parameters steadily converge to certain values. With regard to the parameter f_c, the convergence value was quite small. This was mainly caused by model errors entailed by the Kent-Scott-Park model itself, which cannot take into account a significant influence of shear stresses. Therefore, the UKF method forced the reduction of f_c, the most sensitive parameter, to compensate for model errors. Moreover, in Fig. 23, 'identification results' indicates the displacement-force response computed by the FE model using the online identified parameters via UHS, while the 'FE results with initial values' presents the response using the initial values of parameters as constant in the FE model, i.e. the values of parameters for the NS in the SHS. As a result, the accuracy of the parameter identification can be deduced from the comparison to data measured from the PS, i.e. the testing results. Eventually, Fig. 24 illustrates the comparison of displacement-force responses at the interface between PS and NS of the full-scale pier provided by the SHS and the UHS. One can observe the huge differences between results provided by SHS and UHS. It is evident that UHS can significantly enhance SHS.

In this case, the average execution time is similar to that of the numerical validation case presented in Subsection 3.2. The runtime of both the FE model and data transmission represents the most time consuming modules at each identification step.

4.6.2 Results of the seismic response of the bridge

Given the FE discretization of Fig.14, the lateral displacement histories at the top the two piers, *i.e.* DoF 7 of node 6 and DoF 16 of node 12, were different when the SHS was applied, because that the element 1-2 was taken out testing as the PS, while the element 7-8 was numerically simulated without model updating. However, when the UHS was employed, the displacement histories of DoF7 and DoF16 were expected to be similar, where the parameters of concrete constitutive model in the NS including element 7-8 were updated based on the experimental data of the PS. Fig. 25 presents the corresponding analysis results of the bridge using UHS. As expected, one can observe that time histories of displacement at the top of the two piers were similar.

The comparison of the lateral displacement histories at the top of the left pier, *i.e.* DoF 7, between the SHS and UHS is illustrated in Fig. 26. One can observe that the maximum displacement provided by UHS was smaller than that predicted by SHS. This is because SHS does not predict a realistic damage in NSs. The lateral displacement histories of nodes 2, 4 and 6 of the left pier provided by SHS and UHS are shown in Fig. 27 and Fig. 28, respectively. From the figures and also the analysis based on Fast Fourier Transform, it is found that the main vibration frequency of node 4 obtained by UHS was higher than that obtained by SHS due to the contribution of higher modes to the pier response.

In this respect, the lateral displacements of each mass point along the height of the left pier, i.e node 2, 4 and 6, at the same time are presented in Fig. 29. Curve "Node 2" / "Node 4" /

“Node 6” indicates that the lateral displacement of Node 2 / Node 4 / Node 6 reached the maximum value at the two directions, respectively. One can observe that higher-mode effects can be clearly captured by UHS and modify the amount of inelasticity along each pier height.

Previous research show that, the dynamic behavior of slender tall pier is notably influenced by higher vibration modes [43]. With the contribution of higher modes, the plastic hinge can form in the middle besides at the bottom of a tall pier, and the ultimate displacement at the pier top cannot be the only criteria for assessing the seismic performance of the bridge with tall piers [44]. The comparisons of the SHS and UHS, illustrated in Figs. 26 to 30, show that the results provided by the UHS were more consistent with the previous analysis results than that by the SHS; and the dynamic responses of the bridge simulated by the UHS was closer to the real earthquake responses. Therefore, the conclusion can be drawn that the UHS is superior to the SHS on predicting the impacts of higher modes, and hence on evaluating the seismic behavior of the bridge with slender tall piers.

4.6.3 Failure modes of the PS

The PS sketched in Fig. 19 and characterized by a thin-wall hollow section failed at about 1.5g PGA accompanied by a bending-shear failure mode with dominant shear damage. At the onset of failure, a main wide diagonal crack was observed in the front and back sides of the specimen as shown in Fig. 30; stirrups failed, as depicted in Fig. 31, accompanied by concrete crushing at the bottom of the specimen as well as at the position of the diaphragm as indicated in Fig. 32. The width of the main inclined crack was about 3mm. These failure modes are quite difficult to be captured in a pure numerical setting.

5. CONCLUSIONS

In order to improve the modeling of critical NSs that cannot be tested in a laboratory, and, hence, the overall quality of hybrid simulation, model updating is proposed by means of constitutive laws at the stress-strain level, where the parameters of the concrete constitutive model are online identified and updated during hybrid simulation. The typical requirements that the updated components in the NSs must have the same factors of PSs, which involve constitutive models at the global level, such as boundary conditions, axial ratio, geometric dimensions, etc., can be relaxed. In order to replace the measurement equation, the OpenSees software platform was developed to be embedded into the UKF framework; so, we were able to analytically express the measurement equation. This identification method enlarges the scope of selecting the observation quantity. As a proof of concept, the proposed method was numerically verified on a RC frame and further physically validated by carrying out a number of hybrid simulations with a large-scaled specimen, i.e. the PS, on a large-complex RC rigid frame bridge characterized by thin-wall hollow-section tall piers. The following conclusions can be drawn.

(1) The implementation of the OpenSees-embedded UKF for online identification of concrete constitutive parameters was proven to be accurate, efficient and suitable for HS based on online model updating.
(2) The feasibility of the proposed identification method applied to HS with online model

updating (UHS) is demonstrated by numerical simulations on a RC frame. A further proof of this UHS on a large-complex RC rigid frame bridge is provided. Compared to standard HS without model updating, results show that online updating of concrete constitutive models can significantly improve the accuracy of NS responses, making the high-order frequency responses well captured for a bridge with tall flexural piers. As a result, the HS with updating concrete constitutive parameters is feasible and can be extended to large complex systems endowed with numerous critical members.

(3) The failure mode of a pier endowed with a thin-wall hollow section appears to be of bending-shear type with one main diagonal crack running through the specimen. The specimen was severely damaged by the tensile rupture of stirrups accompanied by concrete crushing at the bottom and at the diaphragm. As a result, the shear influence in RC components with thin-wall hollow sections should be accurately and fully considered in numerical simulations.

Because both specimens and experimental data are limited, improved FE models of bridge components were deterministically obtained without considering material/structural uncertainties as well as seismic input uncertainties. As a result, the effects of uncertainties on the seismic bridge response associated with the variability of model parameters and seismic input deserve further studies.

COMPETING INTERESTS

The authors declare that there is no conflict of interest regarding the publication of this paper.

ACKNOWLEDGEMENTS

The authors gratefully acknowledge the financial supports from the National Key Research and Development Program of China (Grant No. 2016YFC0701106), the National Natural Science Foundation of China (Grant No. 51161120360) and the Specialized Research Fund for the Doctoral Program of Higher Education of China (Grant No. 20132302110065). Moreover, the first author acknowledges the financial support from Seismic Engineering Research Infrastructure for European Synergies (SERIES) Project, funded within the 7th Framework Programme of the European Commission [FP7/2007–2013] under grant agreement no. 227887, for her research period at University of Trento, Italy. The third author acknowledged the Grant No: 730900, Seismology and Earthquake Engineering Research Infrastructure Alliance for Europe (SERA) of the European Commission [HORIZON 2020, 2017-2020]. Finally, the fourth author acknowledges the National Science Foundation of China (Grant No. 51778190).

REFERENCES

[1] Han Q, Du X, Liu J, et al. Seismic damage of highway bridges during the 2008 Wenchuan earthquake [J]. Earthquake Engineering and Engineering Vibration, 2009, 8(2): 263-273.
[2] Delgado R, Delgado P, Pouca N V, et al. Shear effects on hollow section piers under seismic actions: experimental and numerical analysis[J]. Bulletin of Earthquake Engineering, 2009, 7(2): 377.
[3] Ranzo G, Priestley M J N. Seismic performance of large RC circular hollow columns[C]. Proceedings of 12th World Conference on Earthquake Engineering, Auckland, New Zealand, 2000.
[4] Calvi G M, Pavese A, Rasulo A, et al. Experimental and numerical studies on the seismic response of RC hollow bridge piers[J]. Bulletin of Earthquake Engineering, 2005, 3(3): 267-297.
[5] Han Q, Du X, Zhou Y, et al. Experimental study of hollow rectangular bridge column performance under vertical and cyclically bilateral loads, J. Earthquake Engineering and Engineering Vibration, 2013, 12(3): 433-445.
[6] Spencer BF, Chang C-M, Frankie TM, Kuchma DA, Silva PF, Abdelnaby AE. A phased approach to enable hybrid simulation of complex structures. Earthquake Engineering and Engineering Vibration 2014; 13: 63–77.
[7] Pegon P. and Pinto A. V. Pseudo‐dynamic testing with substructuring at the ELSA laboratory [J]. Earthquake engineering & structural dynamics, 2000, 29(7): 905-925.
[8] Terzic V, Stojadinovic B. Hybrid simulation of bridge response to three-dimensional earthquake excitation followed by truck load [J]. Journal of Structural Engineering, 2013, 140(8): A4014010.
[9] Abbiati, G., Bursi, O.S., Caperan P., Di Sarno, L., Molina, F.J., Paolacci, F. and Pegon, P., “Hybrid simulation of a multi-span RC viaduct with plain bars and sliding bearings”, Earthquake Engineering & Structural Dynamics, 2015, 44, 2221–2240
[10] Bursi O.S., Abbiati G., Cazzador, E., Pegon, P. and Molina, F.J., "Nonlinear heterogeneous dynamic substructuring and partitioned FETI time integration for the development of low-discrepancy simulation models", International Journal for Numerical Methods in Engineering, DOI: 10.1002/nme.5556, 2017.
[11] Chuang M. C., S. H. Hsieh, K. C. Tsai, C. H. Li, K. J. Wang, and A. N. Wu, Parameter identification for on-line model updating in hybrid simulations using a gradient-based method[J]. Earthquake Engineering & Structural Dynamics, 2016.
[12] Chen Y., P. Visintin, D. J. Oehlers and U. J. Alengaram, Size-dependent stress-strain model for unconfined concrete. Journal of Structural Engineering, 2013, 140(4): 04013088.
[13] Song W. and S. Dyke, Real-time dynamic model updating of a hysteretic structural system [J]. Journal of Structural Engineering, 2013, 140(3): 04013082.
[14] Hashemi M. J., A. Masroor, and G. Mosqueda, Implementation of online model updating in hybrid simulation. Earthquake Engineering & Structural Dynamics, 2014, 43(3): 395-412.
[15] Wu B. and T. Wang, Model updating with constrained unscented Kalman filter for hybrid testing, Smart Structures and Systems, 2014, 14(6): 1105-1129.
[16] Wu B., Y. Chen, G. Xu, Z. Mei T. Pan, and C. Zeng, Hybrid simulation of steel frame structures with sectional model updating. Earthquake Engineering & Structural Dynamics, 2016, 45:1251-1269.
[17] Kalman R. E. A new approach to linear filtering and prediction problems. Journal of basic Engineering, 1960, 82(1): 35-45.
[18] Erazo K., and Hernandez E.M., A model-based observer for state and stress estimation in structural and mechanical systems: Experimental validation. Mechanical Systems and

Signal Processing, 2014, 43: 141-152.
[19] Sunahara Y. and Yamashita K. An approximate method of state estimation for non-linear dynamical systems with state-dependent noise. International Journal of Control, 1970, 11(6): 957-972.
[20] Julier S. J. and J. K. Uhlmann, New extension of the Kalman filter to nonlinear systems. International Society for Optics and Photonics, 1997.
[21] Julier S. J. and J. K. Uhlmann, A general method for approximating nonlinear transformations of probability distributions. Technical report, Robotics Research Group, Department of Engineering Science, University of Oxford, 1996.
[22] Wan E. A. and R. Van Der Merwe. The unscented Kalman filter for nonlinear estimation. Adaptive Systems for Signal Processing, Communications, and Control Symposium, AS-SPCC, IEEE, 2000.
[23] Hoshiya M. and E. Saito, Structural identification by extended Kalman filter. Journal of Engineering Mechanics, 1984. 110(12): 1757-1770.
[24] Jeen-Shang L. and Z. Yigong, Nonlinear structural identification using extended Kalman filter. Computers & Structures, 1994, 52(4): 757-764.
[25] Chatzi, E.N., Smyth, A.W., and Masri, S.F., Experimental application of on-line parametric identification for nonlinear hysteretic systems with model uncertainty, Journal of Structural Safety, Structural Safety, 2010, 32(5), 326-337.
[26] Kontoroupi K. and Smyth A.W., Online noise identification for joint state and parameter estimation of nonlinear systems. ASCE-ASME Journal of Risk and Uncertainty in Engineering Systems, Part A: Civil Engineering, 2015, 2(3): B4015006.
[27] Chatzis M.N., Chatzi E.N., and Smyth A.W., An experimental validation of time domain system identification methods with fusion of heterogeneous data, Earthquake Engineering and Structural Dynamics, 2015, 44(4), 523-547.
[28] Wu M. and A.W. Smyth, Application of the unscented Kalman filter for real-time nonlinear structural system identification. Structural Control and Health Monitoring, 2007, 14(7): 971-990.
[29] Wu M. and A. Smyth. Real-time parameter estimation for degrading and pinching hysteretic models. International Journal of Non-Linear Mechanics, 2008, 43(9): 822-833.
[30] Chatzi, E., and Smyth, A.W., "The unscented Kalman filter and particle filter methods for nonlinear structural system identification with non-collocated heterogeneous sensing", Structural Control and Health Monitoring, 2009, 16(1), 99-123.
[31] Elanwar H. H., Elnashai A. S., On-line model updating in hybrid simulation tests[J]. Journal of Earthquake Engineering, 2014, 18(3): 350-363.
[32] Astroza R., Ebrahimian H., and Conte J., Material Parameter Identification in Distributed Plasticity FE Models of Frame-Type Structures Using Nonlinear Stochastic Filtering. Journal of Engineering Mechanics, 2014, 141(5): 1-17.
[33] Mei, Z., Wu, B., Bursi, O.S., Yang, G., and Z. Wang. Hybrid simulation of structural systems with online updating of concrete constitutive law parameters by unscented Kalman filter. Structural Control and Health Monitoring, 2017. DOI:10.1002/stc.2069
[34] McKenna F., OpenSEES: A Framework for Earthquake Engineering Simulation, J. Computing in Science & Engineering, 2011, 13(4):58-66.
[35] Doob J. L., Stochastic Processes. New York: Wiley, 1953.
[36] MATLAB and Statistics Toolbox Release. The MathWorks, Inc., Natick, Massachusetts, US. 2012
[37] Kent D. C. and R. Park, Flexural members with confined concrete. Journal of the Structural Division, 1971, 97(7): 1969-1990.
[38] Scott B., R. Park, and M. Priestley, Stress-strain behavior of concrete confined by overlapping hoops at low and high strain rates. Journal Proceedings, 1982.

[39] Mazzoni S., F. Mckenna, M. H. Scott, and G. L. Fenves, OpenSEES command language manual. Pacific Earthquake Engineering Research (PEER) Center, 2006.
[40] Mander J. B., M. J. Priestley and R. Park. Theoretical stress-strain model for confined concrete. Journal of structural engineering, 1988, 114(8): 1804-1826.
[41] Hognestad E., Study of combined bending and axial load in reinforced concrete members. University of Illinois, Engineering Experiment Station, Bulletin No. 399, 1951.
[42] Li B., Research on seismic behavior of continuous rigid frame concrete bridge with high piers and long span. Master's Degree Thesis, Harbin, Institute of Engineering Mechanics, China Earthquake Adiministration, 2011, 17-31.
[43] Tubaldi E, Tassotti L, Dall'Asta A, and L. Dezi. Seismic response analysis of slender bridge piers[J]. Earthquake Engineering & Structural Dynamics, 2014, 43(10): 1503-1519.
[44] Chen X, Li J, X. Liu, Seismic performance of tall piers influenced by higher-mode effects of piers, Journal of Tongji University (Natural Science), 2017, 45(2): 159-166.

Tables

Table 1 Initial and reference values of concrete constitutive parameters

Parameter	f_{cu} (MPa)	ε_{0u}	K	ε_{mu}	K_{sr1}	K_{sr2}	K_{sr3}	f_{yh} (MPa)
Reference value	43	--	--	--	13.5	--	--	579.9
Initial value	43	0.002	0.85	0.0038	13.5	40.5	457.8	--

Table 2 Reference, minimum and maximum values of initial values of parameters

Parameter		f_{cu} (MPa)	ε_{0u}	K	ε_{mu}	K_{sr1}	K_{sr2}	K_{sr3}
Reference value		50	0.002	0.85	0.0035	4.7	14.1	201.4
Variation	Min	50±6	0.002±0.0005	0.2	0.0033	4.2	4.2	185.5
	Max			1	0.0038	5.4	27	213.9

Table 3 Similitude ratios for the PS

	Generalized deformation			Generalized force		
	d_x	d_y	θ	F_x	F_y	M
Ratio of similitude	1/12	1/12	1	$1/12^2$	$1/12^2$	$1/12^3$
Deformations calculated by the COORDINATOR	d_x^c	d_y^c	θ^c	-	-	-
Deformations received by PS	$d_x^c/12$	$d_y^c/12$	θ^c	-	-	-
Forces measured from PS	-	-	-	F_x^p	F_y^p	M^p
Forces received by the COORDINATOR	-	-	-	$12^2 F_x^p$	$12^2 F_y^p$	$12^3 M^p$

Table 4 Parameters for material constitutive models

Parameter	Concrete				Steel	
	f_{cu} (MPa)	ε_{0u}	f_{du} (MPa)	ε_{du}	f_y (MPa)	E_s (MPa)
Pier	40.8	0.002	20.4	2.38	340	2.0×10^5
Girder	33.4	0.002	16.7	2.50	340	2.0×10^5

Table 5 Main frequencies of the RC bridge

Case	Longitudinal direction (Hz)	Vertical direction (Hz)		
	1st	1st	2nd	3rd
Measurement	0.50	1.18	1.90	2.38
Simulation	0.44	1.21	2.06	2.44

Figures

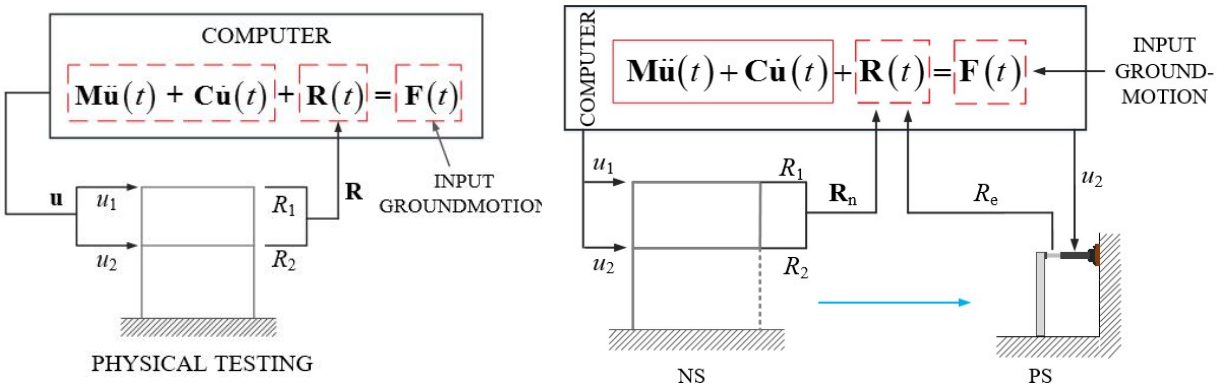

(a) Hybrid simulation of a full system (b) Hybrid simulation with substructures

Fig.1 Schematic of hybrid simulation

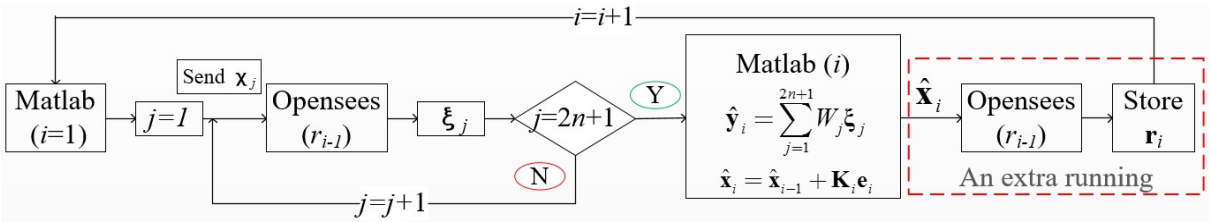

Fig. 2 Flowchart of the identification process at each step

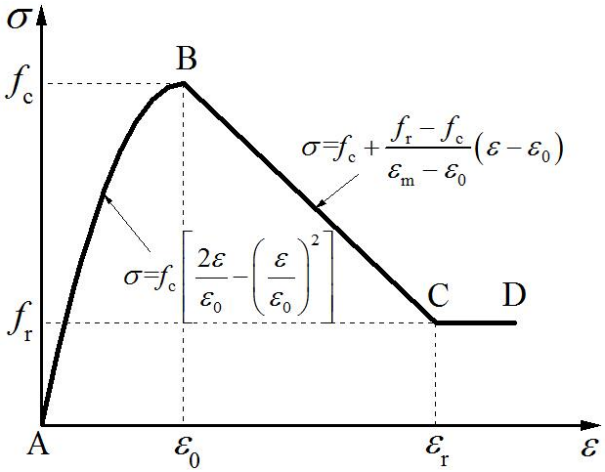

Fig.3 Kent-Scott-Park concrete model available in OpenSees

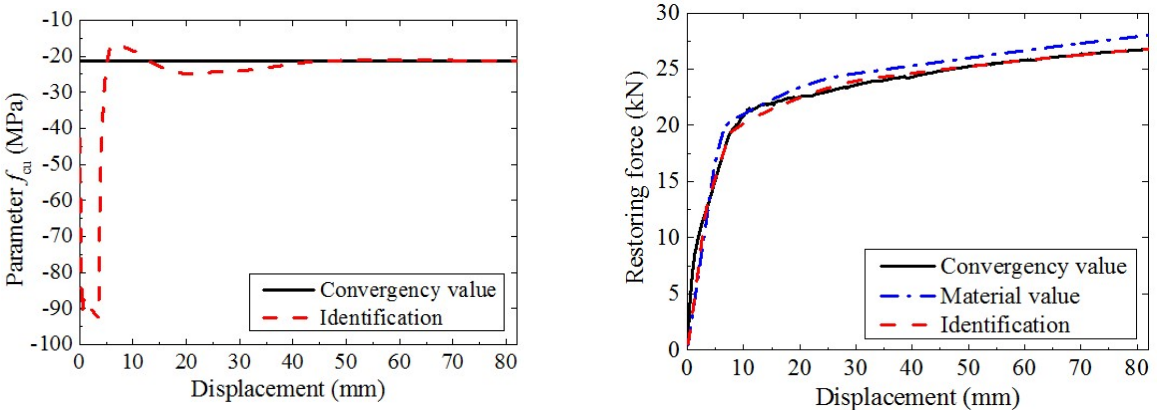

(a) Parameter f_{cu}

(b) Comparison of the displacement-force relations

Fig. 4 Identification results compared with simulated measurements

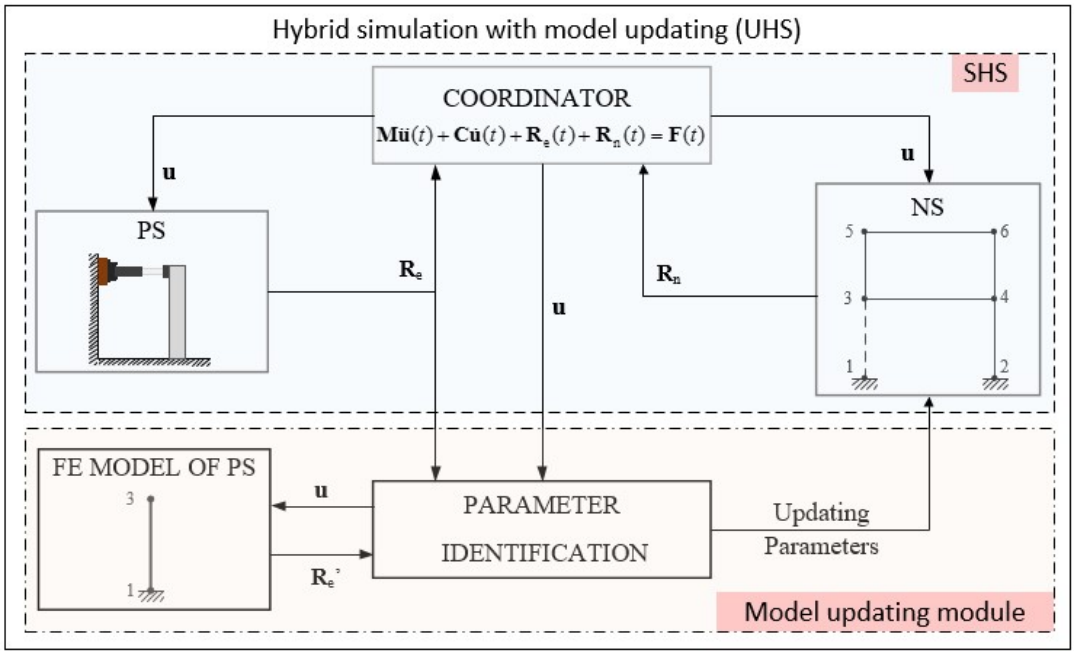

Fig. 5 Schematic of hybrid simulation with model updating

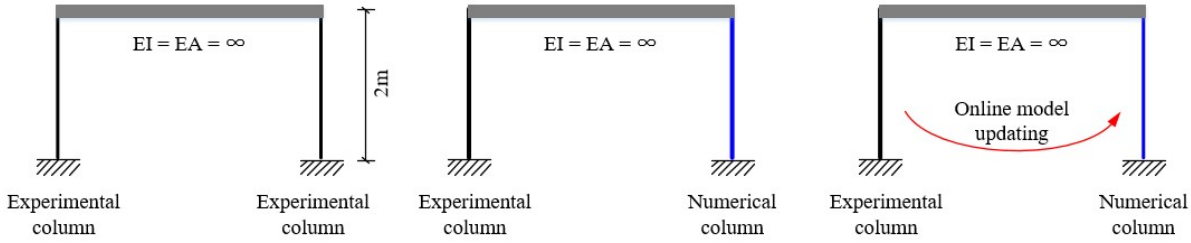

Case A: Reference case

Case B: SHS

Case C: UHS

Fig. 6 Convergence of the identified parameters

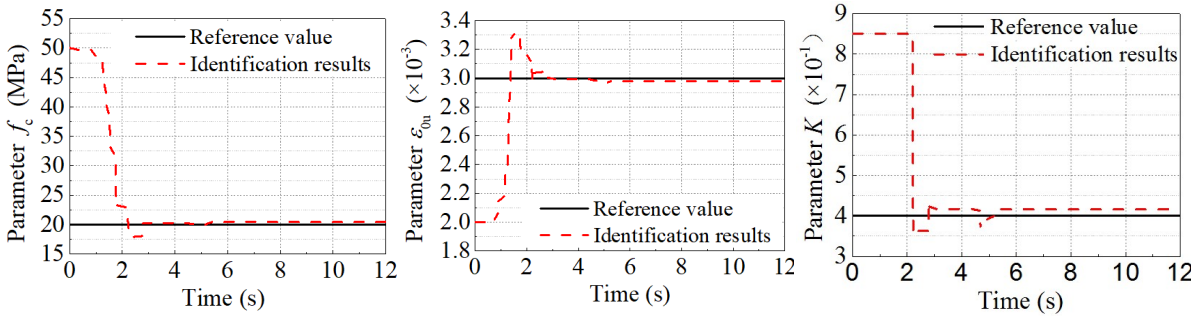

(a) Parameter f_c (b) Parameter ε_0 (c) Parameter K

Fig. 7 Results of parameter identification

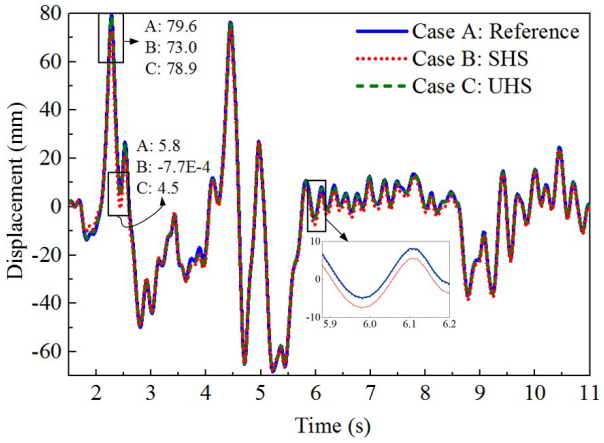

Fig. 8 Displacement time histories at the top of NS column

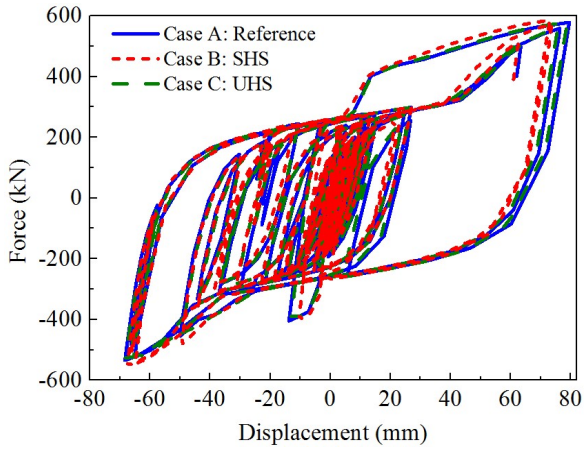

Fig. 9 Displacement-force relationships of the NS

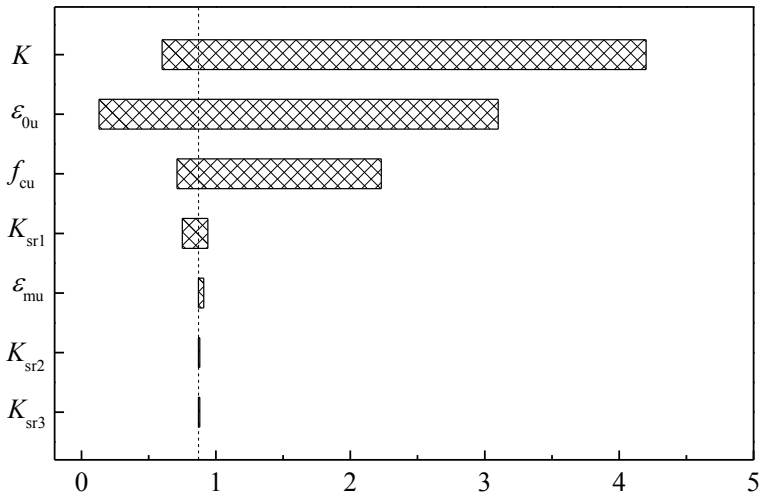

Fig. 10 Bar chart diagram with comparative sensitivity analysis

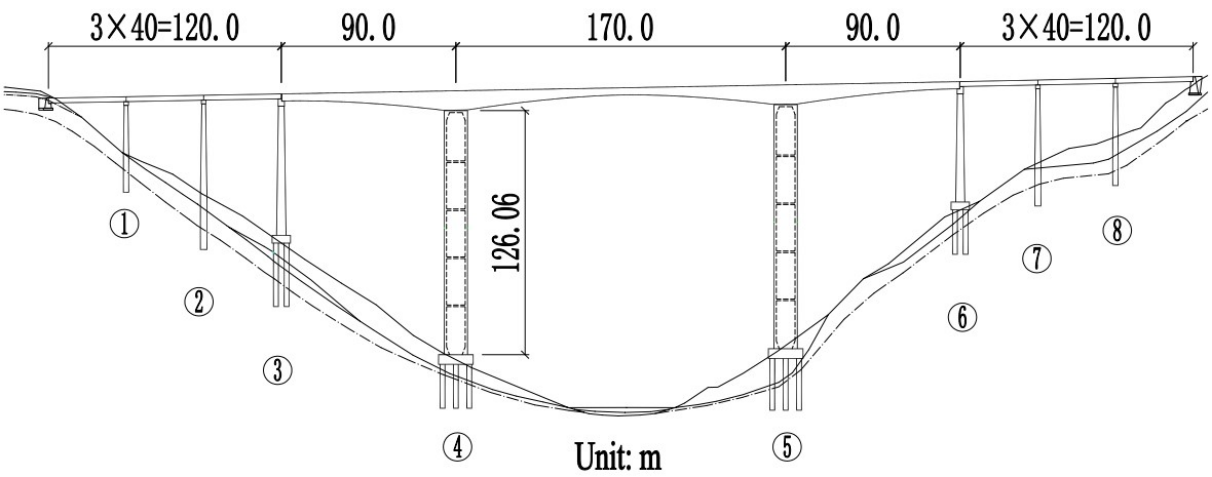

Fig. 11 General arrangement of the prototype RC bridge (Dimensions in m)

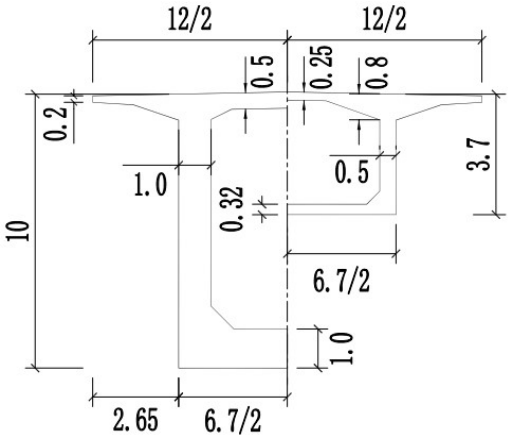

Fig. 12 Cross section of the box girder (Dimensions in m)

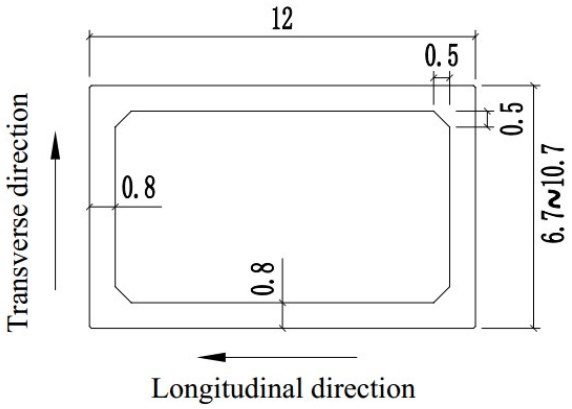

Fig. 13 Cross section of the pier (Dimensions in m)

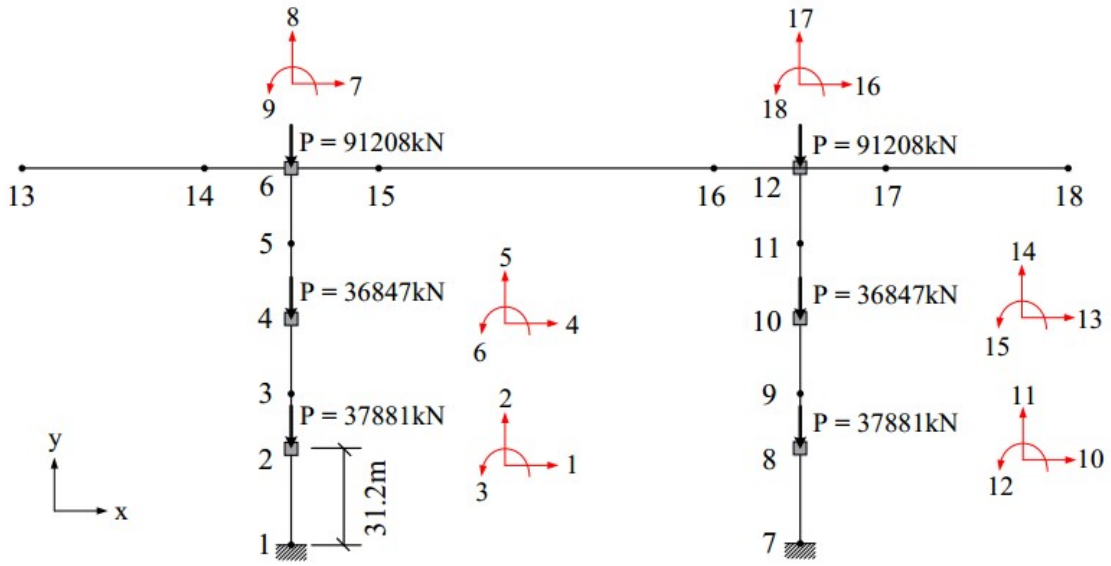

Fig. 14 Analysis model of the main bridge for HSs

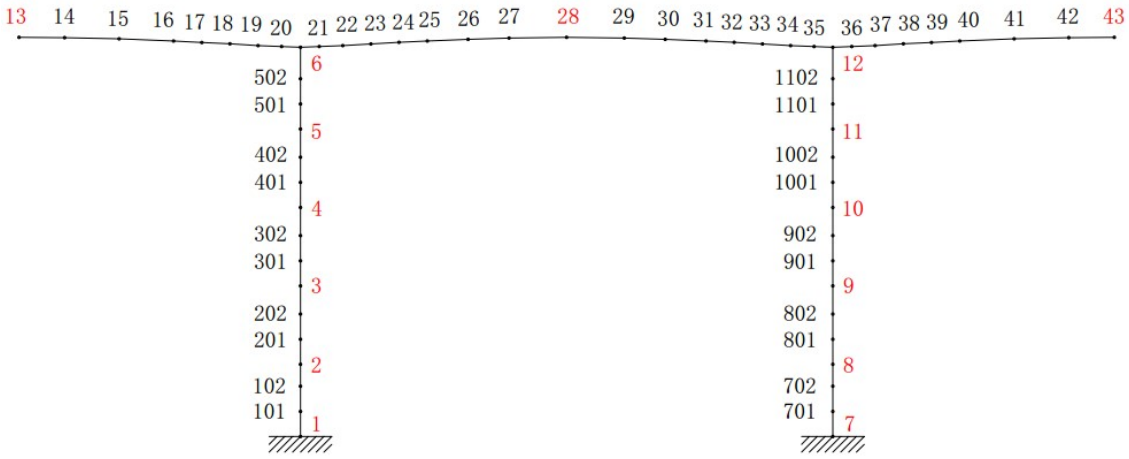

Fig. 15 Schematic of the refined FE model of the main bridge

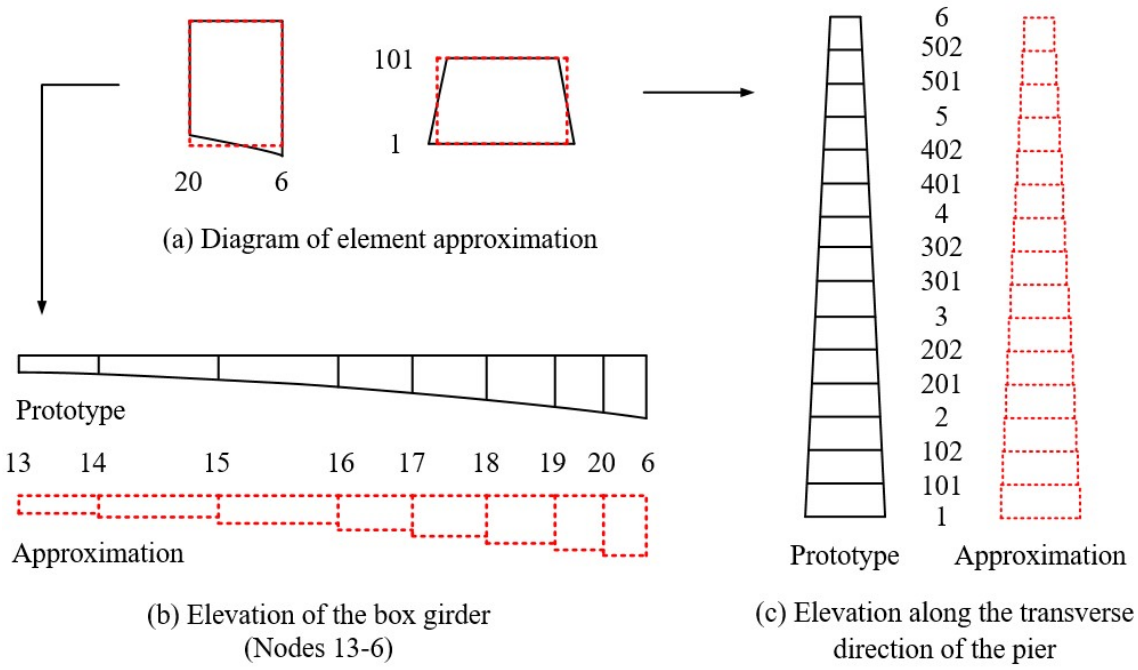

Fig. 16 Sketch of the FE approximate models

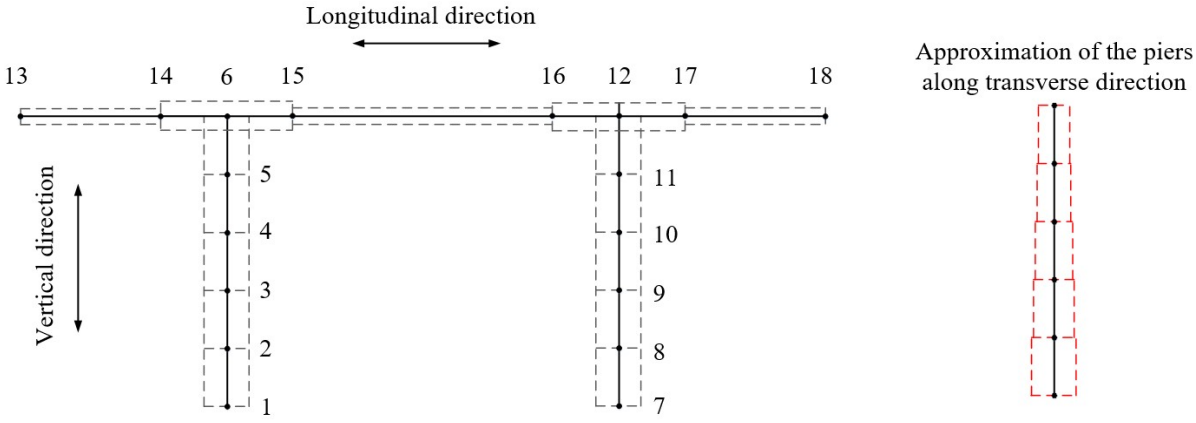

Fig. 17 Simplified FE model of the main bridge

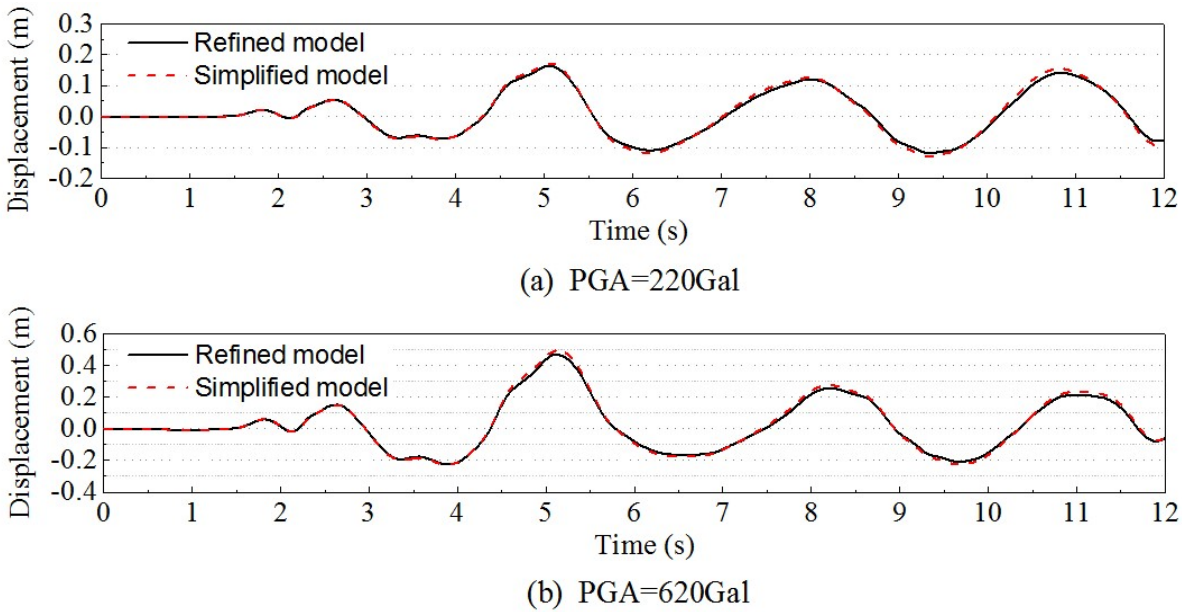

Fig. 18 Displacement-time histories of the main bridge provided by different FE models.

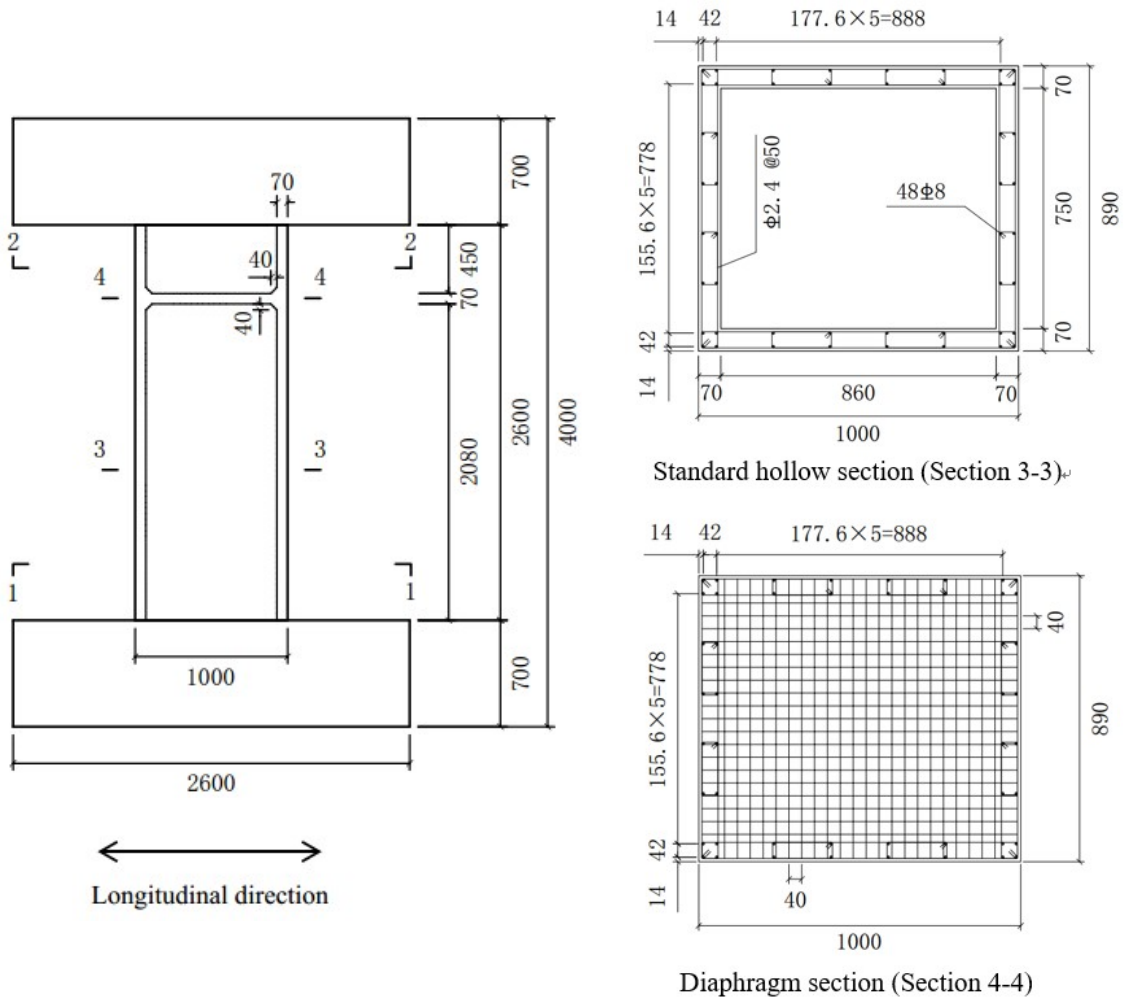

Fig. 19 Dimensions of the specimen PS (in mm)

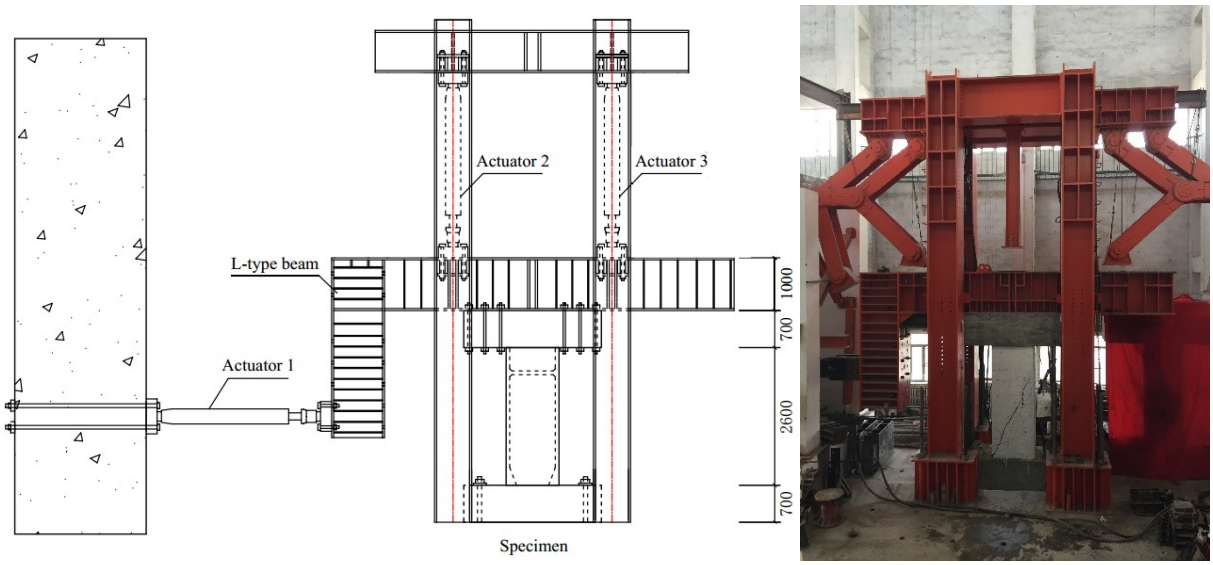

Fig. 20 Loading equipment and the specimen

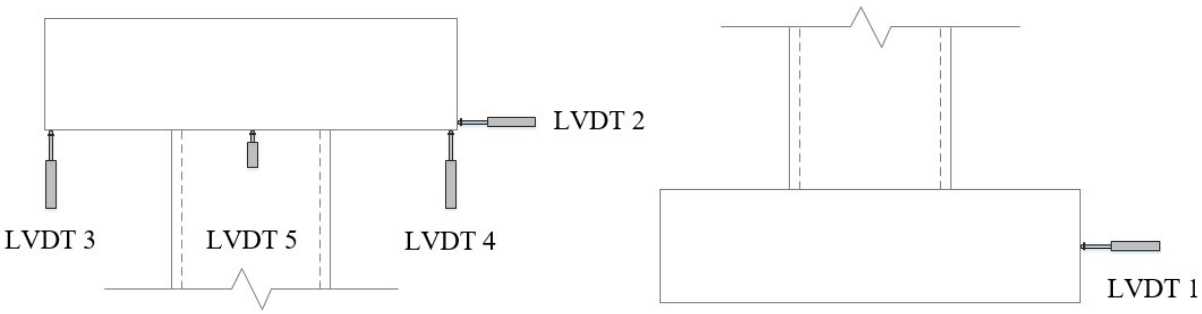

(a) Observation points at the top of the specimen (b) Observation points at the foundation

Fig. 21 Layout of displacement sensors

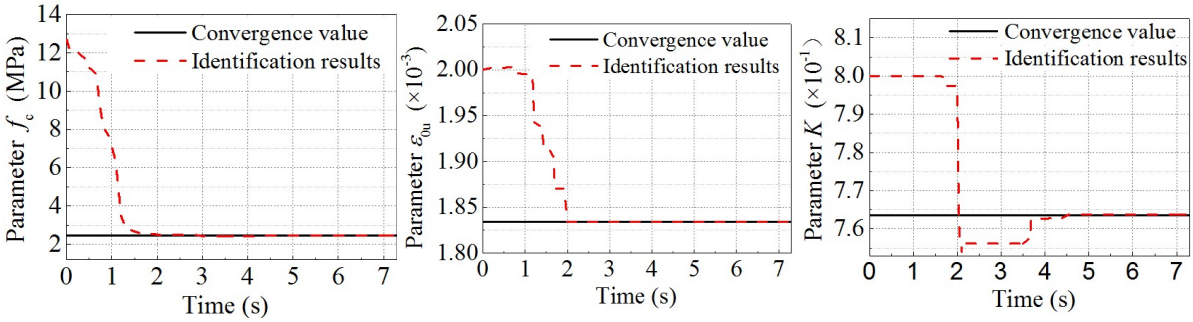

(a) Parameter f_c (b) Parameter ε_0 (c) Parameter K

Fig. 22 Convergence of identified parameters

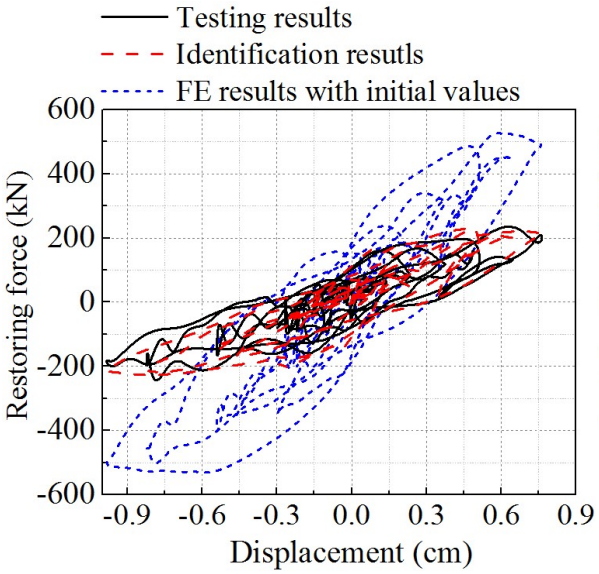

Fig. 23 Comparison of displacement-force responses at the top of the specimen

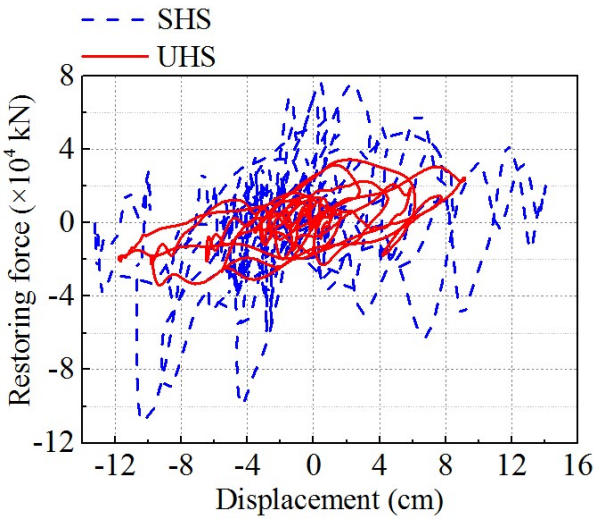

Fig. 24 Comparison of displacement-force responses at the interface between PS and NS of the full-scale pier with standard HS (SHS) and HS with model updating (UHS)

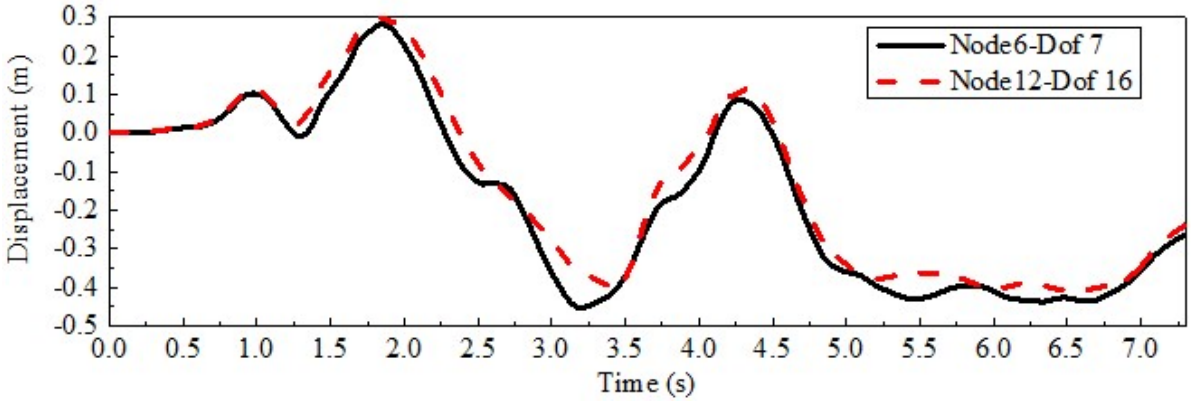

Fig. 25 Displacement histories form the UHS at the top of the two piers

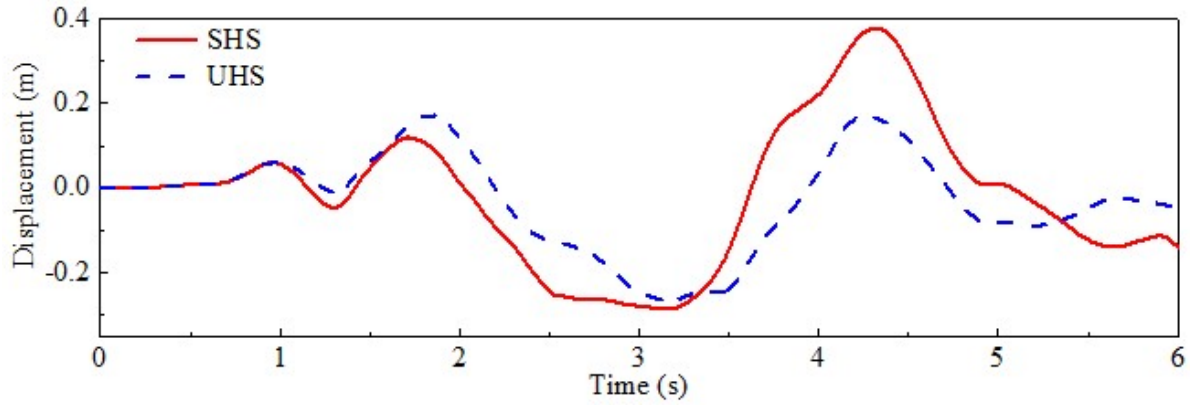

Fig. 26 Displacement histories of the top of the left pier for a PGA = 0.62g

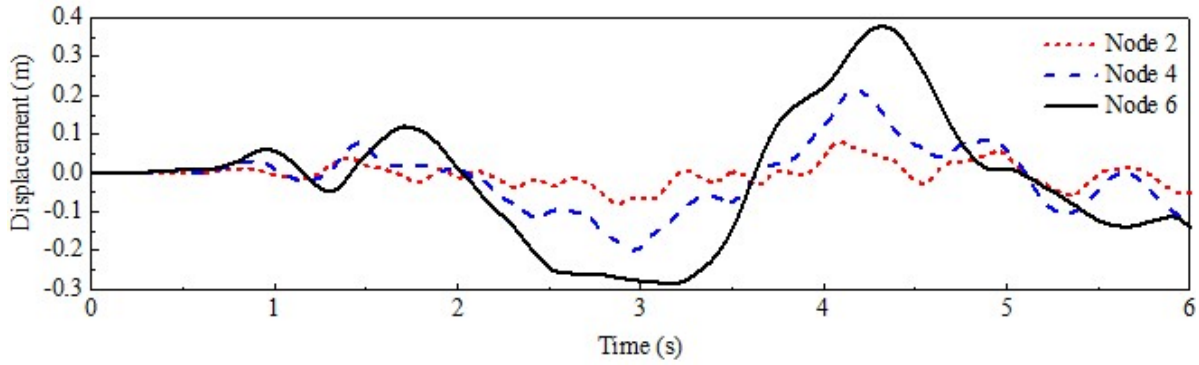

Fig. 27 Lateral displacement histories of node 2, 4 and 6 provided by SHS for a PGA = 0.62g

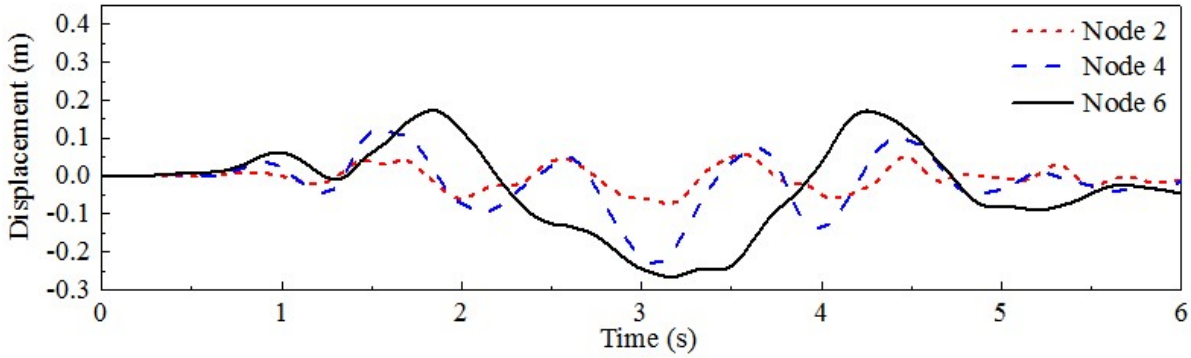

Fig. 28 Lateral displacement histories of node 2, 4 and 6 provided by UHS for a PGA = 0.62g

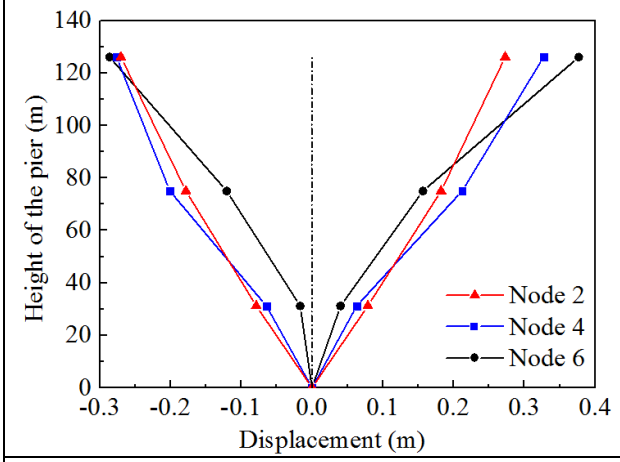

(a) Displacement configuration of masses of left pier provided by SHS

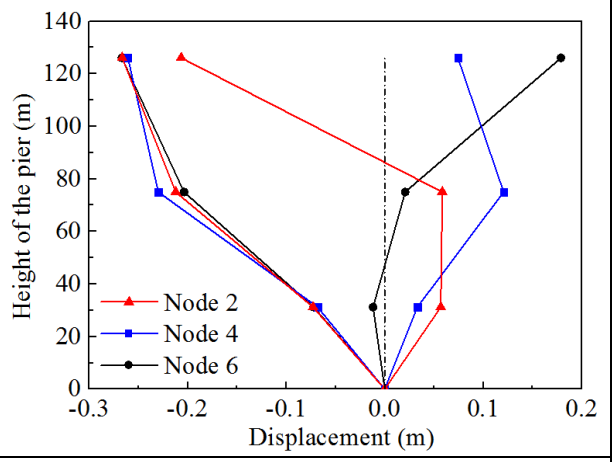

(b) Displacement configuration of masses of left pier provided by UHS

Fig. 29 Lateral displacement of each mass along the height of the pier (PGA = 0.62g)

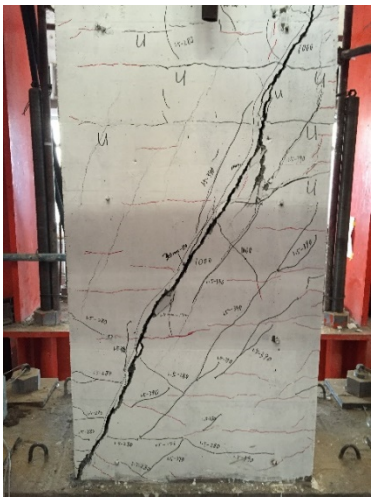

(a) Front view

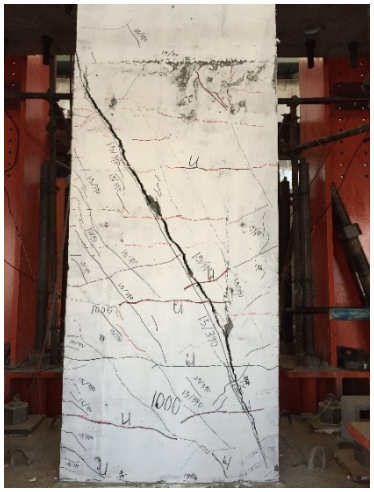

(b) Back view

Fig. 30 Crack distributions along the longitudinal direction

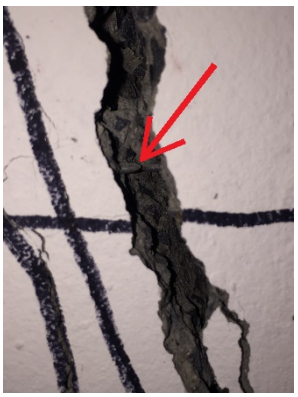

Fig. 31 Rupture of a stirrup due to tensile forces

(a) Bottom of the pier in the left side

(b) Diaphragm failure in the right side

Fig. 32 Concrete crushing of the specimen